

A Continuum Multi-Disconnection-Mode Model for Grain Boundary Migration

Chaozhen Wei^{a,b}, Spencer L. Thomas^c, Jian Han^c, David J. Srolovitz^{c,d,e}, Yang Xiang^a

^a*Department of Mathematics, The Hong Kong University of Science and Technology, Clear Water Bay, Kowloon, Hong Kong SAR, China*

^b*Institute for Advanced Study, The Hong Kong University of Science and Technology, Clear Water Bay, Kowloon, Hong Kong SAR, China*

^c*Department of Materials Science and Engineering, University of Pennsylvania, Philadelphia, PA 19104-6272 USA*

^d*Department of Mechanical Engineering and Applied Mechanics, University of Pennsylvania, Philadelphia, PA 19104-6272 USA*

^e*Department of Materials Science and Engineering, City University of Hong Kong, Kowloon, Hong Kong SAR, China*

Abstract

We study the Grain Boundary (GB) migration based on the underlying disconnection structure and mechanism. Disconnections are line defects that lie solely within a GB and are characterized by both a Burgers vector and a step height, as set by the GB bicrystallography. Multiple disconnection modes can nucleate, as determined by their formation energy barriers and temperature, and move along the GB under different kinds of competing driving forces including shear stress and chemical potential jumps across the GBs. We present a continuum model in two dimensions for GB migration where the GB migrates via the thermally-activated nucleation and kinetically-driven motion of disconnections. We perform continuum numerical simulations for investigating the GB migration behavior in single and multi-mode disconnection limits in both a bicrystal (under two types of boundary conditions) and for a finite-length GB with pinned ends. The results clearly demonstrate the significance of including the coupling and competing between different disconnection modes and driving forces for describing the complex and diverse phenomena of GB migration within polycrystalline microstructures.

Keywords: Grain boundary dynamics, Disconnection mechanism, Shear-coupling

Email addresses: iasczwei@ust.hk (Chaozhen Wei), srol@cityu.edu.hk (David J. Srolovitz), maxiang@ust.hk (Yang Xiang)

1. INTRODUCTION

The microstructure of a polycrystalline material can be abstracted as a network of grain boundaries (GBs) – interfaces between differently oriented crystalline grains. Hence, GB migration is synonymous with polycrystalline microstructure evolution. Since the evolution of such microstructures strongly affect many mechanical, thermal and electronic properties of polycrystalline materials (Sutton and Balluffi, 1995), understanding GB migration mechanisms, dynamics and kinetics is essential to tailoring the structure and properties of polycrystalline materials.

In conventional capillarity-driven grain growth theory (Mullins, 1956; Hillert, 1965), grain boundary migration is described as motion by mean curvature $v_{\perp} = M_{gb}\gamma\kappa$ (for the isotropic case), where M_{gb} is the temperature-dependent GB mobility, γ is the GB energy density (surface tension) and κ is the GB mean curvature. Grain boundaries migrate in the direction of their local normal such as to reduce the local (and total) GB energy (GB area). In the isotropic case, GBs meet at triple junctions (TJs) with a dihedral angle $2\pi/3$ (assuming they are in or near equilibrium) leading to the famous von Neumann-Mullins relation for grain size evolution in two-dimensions (Von Neumann, 1952; Mullins, 1956) and the MacPherson-Srolovitz formula in three-dimensions (MacPherson and Srolovitz, 2007). There is an extensive literature on applying capillarity-driven GB motion to simulate grain growth using continuum methods (e.g., see (Chen and Yang, 1994; Kinderlehrer et al., 2006; Elsey et al., 2009; Lazar et al., 2010)) and to analyze the results of atomistic simulations (Upmanyu et al., 1998). While the isotropic, capillarity-driven grain boundary migration theory has been widely applied, both GB mobility and GB energy depend on the misorientation between grains and the inclination of the grain boundary plane (Read and Shockley, 1950) (in three dimensions this is a five-dimensional parameter space). The effects of such anisotropy on GB migration and grain growth has also been widely examined (Kazaryan et al., 2000; Upmanyu et al., 2002; Zhang et al., 2005) as has its effects on abnormal grain growth (Rollett et al., 1989; DeCost and Holm, 2017) and grain rotation during migration (Harris et al., 1998; Kobayashi et al., 2000; Upmanyu et al., 2006; Esedoğlu, 2016). However, this generalized capillarity-driven model fails to explain many widely observed GB migration phenomena associated affected by mechanical stresses; for example, stress-driven grain growth (Legros et al., 2008; Jin et al., 2004), grain boundary sliding (Van Swygenhoven et al., 2002; Legros et al., 2008; Schäfer and Albe, 2012), grain rotation

(Jin et al., 2004; Ma, 2004; Shan et al., 2004) and abnormal grain growth (Simpson et al., 1971; Riontino et al., 1979).

While the effects of stress on GB migration have long been recognized (Li et al., 1953; Bainbridge et al., 1954), it is only relatively recently that such stress-coupled GB migration has been recognized as a general phenomenon (Srinivasan and Cahn, 2002; Cahn et al., 2006). In shear-coupled GB migration, the motion of the GB in the direction of its normal (i.e., migration) is coupled to a tangential translation of one grain with respect to the other meeting at the GB. Cahn and Taylor (Cahn and Taylor, 2004; Taylor and Cahn, 2007) proposed a description that couples curvature-driven GB motion to mechanical stresses and describes grain boundary sliding and grain rotation. Zhang and Xiang (2018) developed a continuum model for shear coupling in low-angle GBs in terms of the motion and reaction of the constituent dislocations that constitute the GB structure.

Substantial experimental and atomistic simulation evidence exists for the presence of shear-coupled migration in high-angle GBs (Winning et al., 2001; Gottstein et al., 2001; Winning et al., 2002; Rupert et al., 2009; Molteni et al., 1996, 1997; Hamilton and Foiles, 2002; Chen and Kalonji, 1992; Shiga and Shinoda, 2004; Sansoz and Molinari, 2005; Trautt et al., 2012; Homer et al., 2013). Zhang and Xiang (2018) developed a continuum model for shear coupling in low angle GBs in terms of the motion and reaction of the constituent dislocations that constitute the GB structure. Recent experiments and simulations demonstrated that the shear-coupling of high-angle GBs (Rajabzadeh et al., 2013a,b; Momprou et al., 2015) is associated with the motion of line defects known as disconnections (Bollmann, 1970; Ashby, 1972; Hirth and Pond, 1996). Disconnections are constrained to lie within the GB and are characterized by both a Burgers vector \mathbf{b} and a step height H . The motion of disconnections along the GB leads to both GB migration (associated with the step height) and shear coupling (associated with the Burgers vectors) (Thomas et al., 2017; Han et al., 2018). Recently, a continuum model for GB migration was proposed based upon the motion of a single type of disconnection (Zhang et al., 2017). However, bicystallography allows for an infinite, discrete set of possible disconnection types or modes (King and Smith, 1980; Han et al., 2018). A disconnection mode is associated with a Burgers vector and step height pair $\{\mathbf{b}_n, H_{nj}\}$; for each Burgers vector \mathbf{b}_n there are an infinite set of possible step heights $\{H_{nj}\}$. The selection of and competition between disconnection

modes are central to understanding the temperature-dependence of GB shear coupling, mobility, and sliding (Thomas et al., 2017; Han et al., 2018; Chen et al., 2019). Such competition varies between GBs and even along a GB within a microstructure, resulting in complex/rich GB migration phenomenon in polycrystalline microstructures.

In the present paper, we propose a continuum formulation for GB dynamics that accounts for the complexity/richness associated with multiple disconnection modes and apply it by performing continuum simulations that elucidate the interplay between disconnection mode selection, mechanical boundary conditions, driving forces and temperature during GB migration. In order to validate the predictions, we compare these predictions with atomistic (molecular dynamics, MD) simulation results (Thomas et al., 2017). This paper is organized as follows. In Section 2, we present a continuum model for GB migration based upon multiple disconnection modes. Next, we discuss the treatment of the resulting elasticity problem in a bicrystal with prescribed boundary conditions. In Section 3, we perform simulations of shear-coupled GB migration in a bicrystal with two different types of boundary conditions as a function of temperature and in a finite-length GB (e.g., a GB constrained by triple junctions). Finally, in Section 4, we discuss the implication of these results and identify some outstanding questions in GB dynamics in real microstructures.

2. MATHEMATICAL MODEL

2.1. Grain Boundary Motion with Multiple Disconnection Modes

Consider a GB of general shape $y = h(x, t)$, as shown in Fig. 1. Assuming that the GB profile deviates only slightly from that of a reference GB (i.e., a flat GB with its normal parallel to the y -axis), $|\partial_x h| \ll 1$, we may describe the GB profile in terms of an array of disconnections with Burgers vector along the x -direction and step height along the y -direction. (Note, the GB, in its reference configuration has its own structure as described by a combination of structural units with a small period along the x -axis (Sutton and Balluffi, 1995; Han et al., 2017).) In the disconnection mechanism of GB migration, the GB migration rate is controlled by the motion of disconnections along the GB (we focus on disconnection glide here and do not explicitly consider disconnection climb, although there are circumstances for which it is important). When only one disconnection mode is operating, a positive disconnection (\mathbf{b}, H) gliding in the $+x$ direction

(or a negative disconnection $(-\mathbf{b}, -H)$ gliding in the $-x$ direction) will move the GB segment in its wake down by H and shift the top grain with respect to the bottom grain by b (the Burgers vector parallel to the x -direction). In this way, GB migration is coupled with the lateral shear translation of one grain with respect to the other meeting at the GB; this is disconnection-mediated, shear-coupled GB migration.

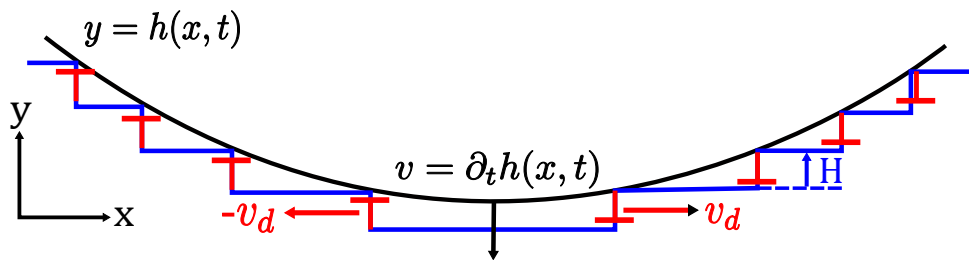


Figure 1: A schematic illustration of shear-coupled migration of a general (small slope) curved GB via the motion of disconnections. The normal migration of the GB, with velocity v (in the y -direction), is achieved by disconnection glide motion with velocity v_d (in the x -direction).

A continuum model for GB migration via the glide of a single disconnection mode was previously proposed (Zhang et al., 2017). Here, we generalize the description of GB motion to account for multiple disconnection modes (including the competition between these modes). Suppose that the GB ($y = h(x, t)$) in Fig. 1 contains multiple disconnection modes (\mathbf{b}_n, H_{nj}) with $\mathbf{b}_n = (b_n, 0)$ parallel to the x -axis and H_{nj} parallel to the y -axis, where n is the Burgers vector index and j represents one of the allowed step heights corresponding to \mathbf{b}_n . For simplicity, and without loss of generality, we write the set of possible disconnection modes as $\{\mathbf{b}_i, H_i\}$ where the subscript i is the disconnection mode index. The disconnection density ρ_i is positive/negative to represent the density of disconnection of type $(\mathbf{b}_i, H_i)/(-\mathbf{b}_i, -H_i)$. GB migration may now be described in terms of the disconnection flux J_i

$$\frac{\partial h}{\partial t} = - \sum_i J_i H_i. \quad (1)$$

A continuity condition insures conservation of Burgers vector and step height

$$\frac{\partial \rho_i}{\partial t} + \frac{\partial J_i}{\partial x} = 0. \quad (2)$$

The disconnection flux J_i is defined as

$$J_i = v_i(|\rho_i| + 2c_i), \quad (3)$$

where v_i is the glide velocity of a positive disconnection and c_i is the thermal equilibrium concentration of disconnections of type i . The latter term represents a model for disconnection nucleation (Zhang et al., 2017)

$$c_i = \frac{1}{a} e^{-E_i^*/(k_B T)}, \quad (4)$$

where a is an atomic spacing, k_B is the Boltzmann constant, T is temperature and E_i^* is half of the formation energy of a disconnection pair (Han et al., 2018). We assume that disconnection nucleation is sufficiently facile that the nucleation rate is determined by thermal equilibrium considerations (this may not be universally valid). The relation between the GB shape and disconnection density is simply $\partial_x h = \sum_i \rho_i H_i$ (consistent with Eqs. (1)-(2)). During shear-coupled GB migration, disconnection glide induces a shear translation between the two grains meeting at the GB. The relative grain translation (GB sliding) rate $\partial_t B$ and the shear coupling factor are related to the disconnection flux

$$\partial_t B = \sum_i J_i b_i, \quad (5)$$

$$\beta = \partial_t B / \partial_t h, \quad (6)$$

where β is the shear coupling factor defined as the ratio of the grain translation rate and the GB migration rate and is an important descriptor of shear-coupled GB migration.

We assume that disconnection motion is overdamped, such that disconnection velocity is proportional to the driving force. For a disconnection of mode (\mathbf{b}, H) , $v_d = M_d \cdot f_d$, where M_d is the disconnection mobility and f_d is the total driving force on this disconnection. The driving force consists of two parts $f_d = f_b + f_h$, where f_b is the force conjugate to the Burgers vector and f_h to the step character. The driving force associated on the disconnection associated with a stress is the Peach-Koehler force (Peach and Koehler, 1950) along the glide direction, i.e., $f_b = [(\boldsymbol{\sigma} \cdot \mathbf{b}) \times \boldsymbol{\xi}] \cdot \mathbf{g}$, where $\boldsymbol{\sigma}$ is the local stress (tensor), $\boldsymbol{\xi}$ is the disconnection line direction (perpendicular to the x - y plane) and \mathbf{g} is the glide direction (i.e., x). The driving force associated with the step character is related to the jump in chemical potential across the GB, i.e., $f_h = (\Psi - \gamma \partial_{xx} h) H$ where Ψ is the difference between the energy densities in two grains meeting at a GB (e.g., the synthetic driving force widely used in atomistic simulations of GB migration) and where we have explicitly separated out the contribution to the chemical potential jump associated with capillarity (γ is the GB energy and $\partial_{xx} h$ is the GB mean curvature). These

driving forces can be derived directly from the variation of the total energy of the system with respect to the virtual displacement of the disconnection along the GB; i.e., f_b and f_h correspond to the variation of the (long-range interaction) elastic energy and the non-elastic contributions to the energy associated with disconnection motion. Inserting these forces into the expression for the disconnection velocity yields

$$v_d = M_d[(\sigma + \tau)b + (\Psi - \gamma\partial_{xx}h)H], \quad (7)$$

where σ and τ are shear components of the internal and applied stress. Equations (2-7) represent a closed system.

Combining Eqs. (1,3,7) yields an equation of motion for the GB migration with multiple disconnection modes

$$\frac{\partial h}{\partial t} = - \sum_i M_i[(\sigma + \tau)b_i + (\Psi - \gamma\partial_{xx}h)H_i](|\rho_i| + 2c_i)H_i, \quad (8)$$

where M_i is the mobility of a disconnection of mode i . While different disconnection modes will, in general, have different mobilities (with different temperature dependency), for the sake of simplicity of presentation, here we assume that all disconnections have the same, constant mobility $M_i = M_d$. (Disconnection mobilities will, in general, be temperature-dependent with activation energies that depend on disconnection type, local bonding, GB structure, solute segregation, point defects, etc.) Note that the expression for the GB velocity does not explicitly depend on a GB mobility. In other words, rather than the GB velocity simply being the product of the driving force on the GB and a GB mobility, it is determined by the properties of the disconnections (i.e., their mobilities AND their Burgers vector and step height) and their densities along the GB.

The relative importance of the different disconnection modes depends on their relative ease of nucleation under the local conditions, as represented by the parameter c_i in Eq. (8) and dependent on both disconnection formation energy E_i^* and temperature (see Eq. (4)). The formation energy (per unit length) of a disconnection dipole is $2E_i^* = \tilde{A}|H_i| + \tilde{B}|b_i|^2$ (Han et al., 2018) (for a straight dislocation dipole in a periodic system), where \tilde{A} is the excess energy density due to the step and \tilde{B} includes the disconnection core energy and the elastic interaction energy between the two members of the disconnection pair. The coefficients \tilde{A} and \tilde{B} can be

either estimated analytically based upon a continuum model (Han et al., 2018) or determined by fitting to atomistic simulation (Chen et al., 2019) or experimental results. We note that accurate determination of these values should account for the temperature dependence of the formation energy (LeSar et al., 1989; Yang et al., 2015).

The simultaneous activation of multiple disconnection modes adds complexity to GB migration behavior. Since the disconnection nucleation rate is dependent on both formation energy and temperature, the “apparent” GB mobility will vary between GBs, with temperature, and with the nature of the driving force for GB migration (Chen et al., 2019). We explicitly consider the example of $\Sigma 13$ and $\Sigma 37$ symmetric tilt GBs in Cu. For these GBs, simple analysis of the crystallography (Han et al., 2018) shows that for the $\Sigma 13$ GB, $b_n = na_0/\sqrt{26}$ and $H_{nj} = -(5n + 13j)a_0/2\sqrt{26}$ and for the $\Sigma 37$ GB, $b_n = na_0/\sqrt{74}$ and $H_{nj} = (6n - 37j)a_0/2\sqrt{74}$. We extract the values of \tilde{A} and \tilde{B} from Han et al. (2018) and Chen et al. (2019): $\tilde{A}_{\Sigma 13} = 0.48$ and $\tilde{A}_{\Sigma 37} = 0.53$ J/m² and $\tilde{B}_{\Sigma 13} = 42$ and $\tilde{B}_{\Sigma 37} = 36$ GPa. Figure 2 shows the formation energies E_{nj}^* and nucleation rates c_{nj} for these two GBs (as a function of temperature).

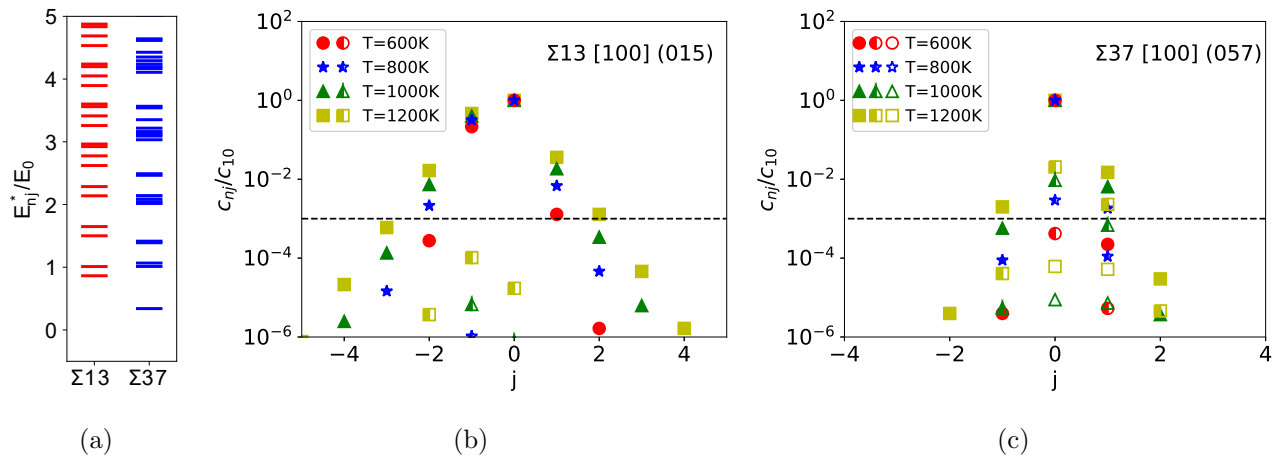


Figure 2: Formation energy and nucleation rates of possible disconnection modes of $\Sigma 13$ and $\Sigma 37$ STGBs in Cu. (a) The formation energy E_{nj}^* of disconnection modes (b_n, H_{nj}) for $n = 1, 2, \dots$ and $j = 0, \pm 1, \pm 2, \dots$, where $E_0 = \tilde{A}a_0$ sets the overall energy scale and a_0 is the lattice constant. (b) and (c) Nucleation rates c_{nj} of disconnection modes (b_n, H_{nj}) at $T = 600, 800, 1000, 1200$ K for $\Sigma 13$ and $\Sigma 37$ GBs, respectively. Filled, half-filled and empty symbols represent disconnection modes with $n = 1, 2,$ and 3 , respectively. The disconnection modes with $n > 3$ have smaller nucleation rates and are beyond the range of this figure. The horizontal dashed line ($c_{nj}/c_{10} = 10^{-3}$) is an arbitrary scale that is used to indicate the relative importance of different disconnection modes.

The disconnection mode (b_1, H_{10}) has the largest nucleation rate c_{10} (lowest formation energy) and hence makes the primary contribution to the shear-coupled GB migration at low temperature, while other disconnection modes, with much smaller nucleation rates, compared to the primary disconnection mode make much smaller contributions (at least at low temperature). As shown in Figs. 2(b) and 2(c), the disconnection modes above the horizontal dashed line (arbitrarily set to $c_{nj}/c_{10} > 10^{-3}$) are considered to be significant during shear-coupled GB migration; while those disconnection modes below the dashed line ($c_{nj}/c_{10} < 10^{-3}$) are considered relatively insignificant here.

For the $\Sigma 37$ GB (Fig. 2(c)), at low temperature ($T = 600$ K) the primary disconnection mode (c_{10}) dominates the shear-coupled GB migration ($c_{nj}/c_{10} < 10^{-3}$ for the other modes), and hence the corresponding coupling factor of the GB migration should be $\beta \simeq -b_1/H_{10}$. At higher temperatures, in addition to the primary disconnection mode, other disconnection modes become significant (with higher formation energy $c_{nj}/c_{10} > 10^{-3}$) and are expected to play a role during GB migration. In contrast, shear-coupled GB migration of the $\Sigma 13$ GB at low temperature ($T = 600$ K) will be governed by two disconnection modes, c_{10} and $c_{1\bar{1}}$ (where bars over indices indicates negative values) as shown in Fig. 2(b), owing to the small gap between the formation energies of these two disconnection modes (see Fig. 2(a)).

When multiple disconnection modes make significant contributions to GB migration, the shear coupling is not determined by a single disconnection mode but rather the average effect of all operating disconnection modes in response to all local driving forces (Thomas et al., 2017; Chen et al., 2019). In general, the coupling factor β for shear-coupled GB migration depends on the mode-specific properties of the disconnection, types of driving forces, and temperature, subject to environment constraints (e.g., mechanical boundary conditions). The present model for GB migration based upon multiple disconnection modes enables us to describe the diverse shear coupling behavior of GB migration associated with the competition between these disconnection modes. For example, it can be applied to interesting high temperature phenomena as pure grain boundary sliding ($\beta \rightarrow \infty$) and pure GB migration without shear deformation ($\beta \rightarrow 0$) which cannot be captured by the single disconnection model for GB migration (Zhang et al., 2017).

2.2. Boundary Conditions

In real polycrystalline microstructures, each grain is confined by surrounding grains and each GB is delimited by junctions with three other GBs (triple junctions, TJs); hence, migration of individual GBs is influenced by other GBs and TJs. Shear displacements that accompany GB migration propagate within the grains, but limited by constraints associated with other grains. Disconnections cannot, in general, be transmitted through TJ. These constraints can result in stress generation and accumulation within grains and/or at TJs during shear-coupled GB migration in the polycrystal. The complexity of polycrystalline systems hinders the complete analysis of these constraints on GB migration. Here, we probe the effects of the constraints by investigating the migration of individual GBs in bicrystals with imposed boundary conditions at the top and bottom surfaces (this provides an analog to the constraints imposed from other grains) or in a finite-length GB with pinned ends (an analog to TJ constraints). For the former case, we consider two types of bicrystal boundary conditions.

Consider a bicrystal (see Fig. 3) that is periodic in the horizontal direction (along x) and bounded in the vertical direction (along y) by top and bottom surfaces. We examine shear-coupled GB migration under free-surface and fixed-surface boundary conditions (BCs). Different

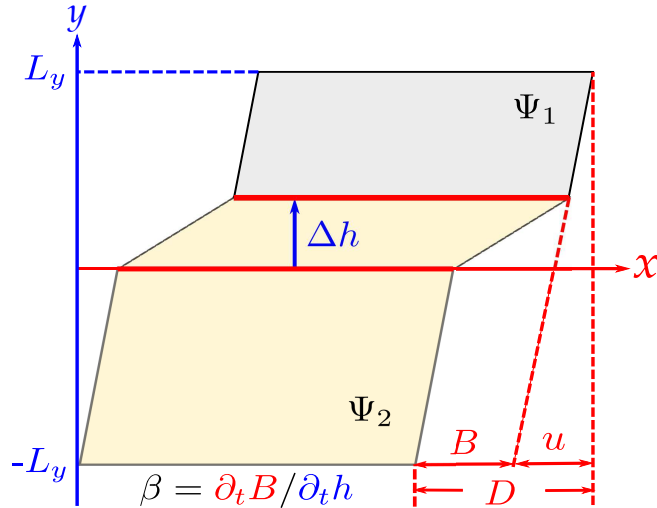


Figure 3: A schematic illustration of shear-coupled GB migration within a bicrystal. When the GB migrates by Δh , the relative translational displacement between the top ($y = L_y$) and bottom ($y = -L_y$) surfaces is $D = B + u$, where u is the elastic deformation and B is the “plastic” deformation (grain translation) induced by the glide of disconnections along GBs.

boundary conditions generate different stresses that may drive disconnection motion and hence affect GB migration. In other words, the effects of the BCs on the GB migration are embodied in image stresses contained in the internal stress field $\boldsymbol{\sigma}$ in Eq. (7). To calculate the internal stress field, we first solve the appropriate elasticity problem in a bicrystal with prescribed BCs.

We use the superposition approach previously employed by Van der Giessen and Needleman (1995) to obtain the internal stress field. Suppose the bicrystal domain Ω (with disconnections distributed along the GB) is a rectangle that extends periodically along the x -direction and is bounded by a top Γ_1 ($y = L_y$) and bottom surface Γ_2 (at $y = -L_y$); see Fig. 4. Consider the following BCs on the elastic displacements/surface tractions on Γ_1 and Γ_2 :

$$\begin{aligned} \mathbf{u} &= \mathbf{u}_1 \quad \text{or} \quad \mathbf{T} = \mathbf{T}_1, & \text{on } \Gamma_1, \\ \mathbf{u} &= \mathbf{u}_2 \quad \text{or} \quad \mathbf{T} = \mathbf{T}_2, & \text{on } \Gamma_2. \end{aligned} \tag{9}$$

Since we assume linear (isotropic) elasticity in the bicrystal domain (Ω), application of the superposition principle allows us to decompose the stress ($\boldsymbol{\sigma}$), strain ($\boldsymbol{\epsilon}$) and displacement (\mathbf{u})

$$\begin{array}{ccc} \begin{array}{c} u = u_1, T = T_1 \text{ on } \Gamma_1 \\ \sigma = \tilde{\sigma} + \hat{\sigma} \\ \epsilon = \tilde{\epsilon} + \hat{\epsilon} \\ u = \tilde{u} + \hat{u} \\ \Omega \\ u = u_2, T = T_2 \text{ on } \Gamma_2 \end{array} & = & \begin{array}{c} \tilde{u}_1, \tilde{T}_1 \text{ on } \Gamma_1 \\ \nabla \cdot \tilde{\sigma} = 0 \\ \tilde{\sigma} = C : \tilde{\epsilon} \\ \int_{C_i} d\tilde{u} = b_i \\ \mathbf{R}^2 \\ \tilde{u}_2, \tilde{T}_2 \text{ on } \Gamma_2 \end{array} & + & \begin{array}{c} \hat{u} = u_1 - \tilde{u}_1, \hat{T} = T_1 - \tilde{T}_1 \text{ on } \Gamma_1 \\ \nabla \cdot \hat{\sigma} = 0 \\ \hat{\sigma} = C : \hat{\epsilon} \\ \Omega \\ \hat{u} = u_2 - \tilde{u}_2, \hat{T} = T_2 - \tilde{T}_2 \text{ on } \Gamma_2 \end{array} \end{array}$$

Figure 4: Decomposition of the elasticity problem in a domain Ω containing disconnections with prescribed BC on Γ_1 and Γ_2 and periodic BCs on the left and right edges. The solution (σ, ϵ, u) to the elasticity problem in Ω containing disconnections is the superposition of the fields $(\tilde{\sigma}, \tilde{\epsilon}, \tilde{u})$ generated by the disconnections in an infinite medium \mathbf{R}^2 , and the solution $(\hat{\sigma}, \hat{\epsilon}, \hat{u})$ to an elasticity problem in a disconnection-free domain Ω with complementary BCs on Γ_1 and Γ_2 .

fields into two sets as illustrated in Fig. 4

$$\boldsymbol{\sigma} = \tilde{\boldsymbol{\sigma}} + \hat{\boldsymbol{\sigma}}, \quad \boldsymbol{\epsilon} = \tilde{\boldsymbol{\epsilon}} + \hat{\boldsymbol{\epsilon}}, \quad \mathbf{u} = \tilde{\mathbf{u}} + \hat{\mathbf{u}} \quad \text{in } \Omega. \quad (10)$$

Here, the first set of fields $(\tilde{\boldsymbol{\sigma}}, \tilde{\boldsymbol{\epsilon}}, \tilde{\mathbf{u}})$ is generated by all of the disconnections in the infinite medium and a second set of fields $(\hat{\boldsymbol{\sigma}}, \hat{\boldsymbol{\epsilon}}, \hat{\mathbf{u}})$ corresponding to image stresses (associated with the) constraints at the top and bottom surfaces.

The fields $(\tilde{\boldsymbol{\sigma}}, \tilde{\boldsymbol{\epsilon}}, \tilde{\mathbf{u}})$ for a discrete dislocation in an infinite medium are well-known (Hirth and Lothe, 1982, Chap.3). However, since we consider periodic BCs in the horizontal direction, we must account for the fields of the replicas of this discrete dislocation in all periodic cells. The analytical solutions for such a string of dislocations are also known (Hirth and Lothe, 1982; Van der Giessen and Needleman, 1995).

Let $\boldsymbol{\sigma}_i(x - x_0, y - y_0)$ be the stress at point (x, y) generated by a disconnection of mode i located at (x_0, y_0) (in the current cell) and its periodic replicas (see Eq. (A.1)). Similarly, the stress at point (x, y) from all disconnection modes along the GB is now simply

$$\tilde{\boldsymbol{\sigma}}(x, y) = \int_{\mathcal{L}} \sum_i \boldsymbol{\sigma}_i(x - x_0, y - y_0) \rho_i(x_0, y_0) ds, \quad (11)$$

where the integral over s denotes locations (x_0, y_0) along the GB, denoted by \mathcal{L} . We can similarly obtain the corresponding strain and the displacement fields $(\tilde{\boldsymbol{\epsilon}}, \tilde{\mathbf{u}})$.

The fields $(\tilde{\boldsymbol{\sigma}}, \tilde{\boldsymbol{\epsilon}}, \tilde{\mathbf{u}})$ are obtained for disconnections in an infinite medium by ignoring the boundary constraints at the top and bottom surfaces. The associated displacements and surface tractions along the top and bottom surfaces Γ_k ($\tilde{\mathbf{u}}_k, \tilde{\mathbf{T}}_k$), do not necessarily satisfy the prescribed BCs in Eq. (9).

To ensure the total fields $(\boldsymbol{\sigma}, \boldsymbol{\epsilon}, \mathbf{u})$ satisfy the BCs, we introduce a second set of fields $(\hat{\boldsymbol{\sigma}}, \hat{\boldsymbol{\epsilon}}, \hat{\mathbf{u}})$ to be added to the original total fields that satisfy

$$\nabla \cdot \hat{\boldsymbol{\sigma}} = \mathbf{0}, \quad \hat{\boldsymbol{\sigma}} = \mathbf{C} : \hat{\boldsymbol{\epsilon}}, \quad \hat{\boldsymbol{\epsilon}} = \frac{1}{2}[\nabla \hat{\mathbf{u}} + (\nabla \hat{\mathbf{u}})^{\mathbf{T}}] \quad \text{in } \Omega \quad (12)$$

$$\hat{\mathbf{u}} = \mathbf{u}_1 - \tilde{\mathbf{u}}_1 \quad \text{or} \quad \hat{\mathbf{T}} = \mathbf{T}_1 - \tilde{\mathbf{T}}_1, \quad \text{on } \Gamma_1 \quad (13)$$

$$\hat{\mathbf{u}} = \mathbf{u}_2 - \tilde{\mathbf{u}}_2 \quad \text{or} \quad \hat{\mathbf{T}} = \mathbf{T}_2 - \tilde{\mathbf{T}}_2, \quad \text{on } \Gamma_2. \quad (14)$$

This is an elasticity problem in a disconnection-free domain subject to the complementary boundary conditions (the difference between the values of the prescribed BCs and the boundary

values from the original set of fields). This elasticity problem has analytical solutions for a rectangle domain under both free- and fixed-surface BCs.

For free-surface BCs, the tractions along the surfaces are zero ($\mathbf{T}_1 = \mathbf{T}_2 = \mathbf{0}$). We solve for the stress field $\hat{\boldsymbol{\sigma}}$ using an Airy stress function and Fourier analysis. The solutions for the Airy function and stress are given in Eqs. (A.3–A.4).

For the fixed-surface BCs, we set the total displacements to be zero. As shown in Fig. 3, in addition to the elastic displacement \mathbf{u} , the total displacement \mathbf{D} includes the “plastic” displacement \mathbf{B} associated with grain translation, i.e., $\mathbf{D} = \mathbf{u} + \mathbf{B}$. Note that the grain translation Eq. (5) is the relative lateral “plastic” displacement between the top and bottom surfaces. If we define, without loss of generality, a positive disconnection as having a Burgers vector in the $+x$ direction for all disconnection modes ($b_i > 0$ for all i), we may write the lateral “plastic” displacements for the top and bottom surfaces separately as

$$\begin{aligned} B_1 &= \int \sum_i v_i(\rho_i^+ + c_i)b_i dt \quad \text{on } \Gamma_1, \\ B_2 &= \int \sum_i v_i(\rho_i^- - c_i)b_i dt \quad \text{on } \Gamma_2, \end{aligned} \tag{15}$$

where

$$\rho_i^+ = \max(\rho_i, 0), \quad \rho_i^- = \min(\rho_i, 0). \tag{16}$$

To satisfy the fixed-surface BCs in Eqs. (13–14), we set $\mathbf{u}_1 = -\mathbf{B}_1 = (-B_1, 0)$ and $\mathbf{u}_2 = -\mathbf{B}_2 = (-B_2, 0)$. We solve this elastic boundary value problem for the displacement field $\hat{\mathbf{u}}$ by employing a displacement formulation of the equilibrium equation (Eq. (12)) such that $\hat{\mathbf{u}}$ satisfies the biharmonic equation when the body force is zero; see Eq. (A.5–A.6). The stress field $\hat{\boldsymbol{\sigma}}$ is then obtained from the linear elastic constitutive equations.

By applying the superposition approach described above, we determine the internal stress in the GB equation of motion Eq. (8) that includes the effects of the boundary constraints. We now examine the effects of such constraints on GB migration by applying our continuum model to GB migration in a bicrystal under fixed- and free-surface BCs.

3. SIMULATION RESULTS

We apply our continuum model in a series of numerical simulations to study shear-coupled GB migration with multiple disconnection modes as a function of boundary constraints, types of driving forces and temperature. To parameterize this model, we employ the atomistic simulation data for copper using an embedded atom interatomic potential (Mishin et al., 2001): shear modulus $\mu = 45$ GPa, poisson ratio $\nu = 0.36$, and lattice constant $a_0 = 3.615$ Å. Cahn et al. (2006) determine the grain boundary energy densities of several [001] symmetric tilt grain boundaries with this potential: for $\Sigma 13$ (015) $\gamma = 0.878$ J/m² and for $\Sigma 37$ (057) $\gamma = 0.732$ J/m². We also use the following parameters: the disconnection mobility $M_d = 100$ m²/(J·s) and the length of the GB in the bicrystal $L_0 = 100$ Å.

3.1. Grain Boundary Migration in a Bicrystal

We first study GB migration in a bicrystal driven by a jump in chemical potential across the GB (i.e., a synthetic driving force (Janssens et al., 2006)) under free- and fixed-surface BCs at the top and bottom surfaces. Molecular dynamics simulations were previously employed by Thomas et al. (2017) to investigate shear-coupled migration of a flat GB. When free-surface BCs were employed, they observed that GBs readily migrate through the entire bicrystal and the grains show lateral translation with respect to one another, as expected during low temperature, shear-coupled GB migration. However, when fixed-surface BCs were employed at low temperature, the GB migrates a short distance then stagnates. They attributed this stagnation to stress generation during shear-coupled migration with fixed-surface BCs. On the other hand, when fixed-surface BCs were employed at a higher temperature, the GB migrates through the entire bicrystal with no net lateral translation of the two grains. They attributed this change in behavior with temperature to the thermal activation of secondary mode disconnections ($\beta > 0$) with opposite sign shear coupling as compared with that resulting from the primary disconnection mode ($\beta < 0$).

The continuum model enables us to easily switch on/off different disconnection modes to ascertain how GB migration is affected by changing BC-type at low temperature and changing temperature for the fixed-surface BC case. We consider $\Sigma 37$ symmetric tilt GB migration based on a single disconnection mode $(a_0/\sqrt{74}, 3a_0/\sqrt{74})$ for two types of BCs. The GB migration

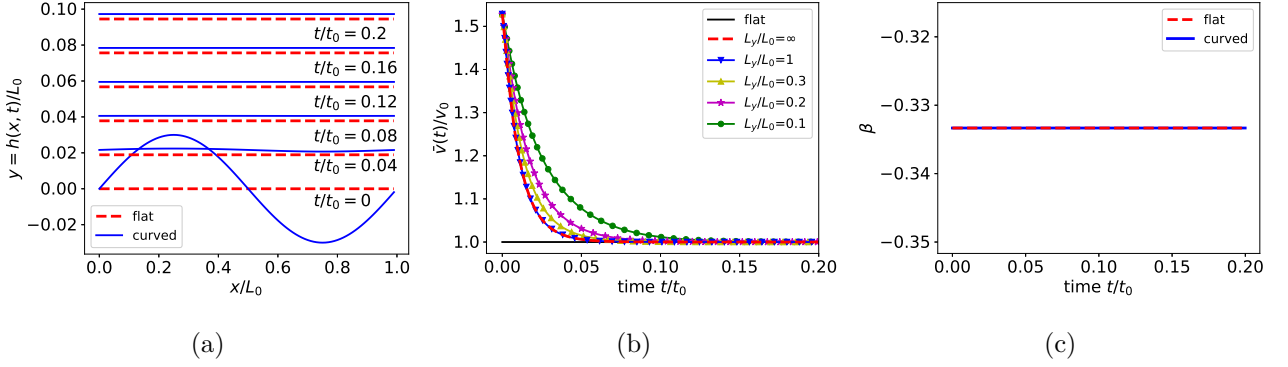


Figure 5: Single-mode migration of a $\Sigma 37$ GB with free-surface BCs at the top and bottom surfaces ($y=\pm L_0$). (a) The migration of an initially flat (red dashed curves) and sinusoidal (solid blue curves) GB under a chemical potential jump driving force $\Psi=-1 \text{ meV}/\text{\AA}^3$. The GBs migrate until they reach the top surface. (b) The average GB velocities $\bar{v}(t)/v_0$ of the initially flat and sinusoidal GBs for several bicrystal lengths in the y -direction, i.e., $L_y/L_0 = 0.1, 0.2, 0.3, 1, \infty$. v_0 is the velocity of the flat GB. (c) The coupling factor of the flat and curved GBs during migration.

results are shown in Fig. 5(a) for the free-surface BC case for both an initially flat and sinusoidal GB. We see that both GBs readily migrate to the end of the bicrystal, driven by a chemical potential jump ($\Psi = -1 \text{ meV}/\text{\AA}^3$). To show the effect of initial GB profile, we examine the average GB migration velocity $\bar{v}(t) = \langle v(x, t) \rangle_x$ (i.e., averaged over position, x in Fig. 5(a)) as a function of time; see Fig. 5(b). While the flat GB migrates at a constant velocity v_0 , the initially sinusoidal GB initially migrates at a larger mean velocity but slows with increasing time as the GB flattens during migration (the initial rate of migration is associated with curved GBs). The difference between the initial migration rates of the flat and sinusoidal GB profiles is attributed to the initial active disconnections along the GB. Both positive and negative disconnections actively glide along the GB (in opposite directions) and lead to GB migration (in the same direction) that results in a non-vanishing average migration velocity, as suggested by the term $|\rho|$ in the GB equation of motion, Eq. 8. While the flat GB has zero local disconnection density everywhere ($\rho = 0$), the sinusoidal GB has a spatially varying disconnection density ($\rho \neq 0$); this implies the sinusoidal GB has more active disconnections and hence a larger initial migration rate. The initially sinusoidal GB slows as it migrates and flattens as the original excess disconnection density relaxes to its steady-state value under the combined driving force of both the elastic interactions between disconnections and capillarity. As the GB approaches

the free surface, the stress field in the bicrystal associated with the zero traction BC slows the flattening. This effect may be understood in terms of the zero traction BC producing effective image disconnections on the other side of the free surface. This image stress field cancels the traction at the free surface and exerts a back stress on the disconnections (associated with the disconnection Burgers vector) along the GB through its associated Peach-Koehler force that prevents disconnection glide associated with GB flattening. This free surface (zero traction or image disconnection) effect is verified by changing the length of the bicrystal (i.e., the simulation cell width in the direction normal to the GB, i.e., L_y), as shown in Fig. 5(b). Decreasing L_y implies slower relaxation of the mean GB velocity. In Fig. 5(c), we verify that the coupling factor of the flat and curved GBs (for every point along the GB) is equal to the coupling factor of the primary disconnection mode, $\beta = -H_{10}/b_{10} = -1/3$.

Figure 6(a) shows the migration of both initially flat and sinusoidal GBs under a chemical potential jump driving force ($\Psi = -1 \text{ meV}/\text{\AA}^3$) for the fixed-surface BCs for bicrystal length $L_y = L_0$. Like in the MD simulations (Thomas et al., 2017), the GBs migrate a short distance and then stagnate at $y/L_0 \approx 6 \times 10^{-2}$. Unlike in the free-surface BC case (where GBs can migrate to the end of the bicrystal cell), the lateral translation of one grain relative to the other during migration is constrained here by the fixed-surface BCs. Hence, as the GB migrates, the stress in the bicrystal accumulates which, in turn, increases the Peach-Koehler force on the disconnections that opposes the driving force associated with the chemical potential jump and hence the GB motion slows, as seen in Fig. 6(b). When the two forces balance, the GB stagnates (see Fig. 7(c)). Moreover, when the GB migration stagnates, the curved GB induces nonuniform shear along the GB (see Fig. 6(d)) and therefore remains (slightly) curved. (The small jogs in $B(x, \infty)$ in this plot are associated with the absolute value of ρ in the disconnection flux, i.e., Eq. (3).) Again, we verify that the coupling factor for GB migration for both the flat and curved GBs is $\beta = -1/3$ (see Fig. 6(c)).

We now examine shear-coupled GB migration for a flat GB where we allow for the possibility of multiple disconnection modes (multi-mode GB migration) with fixed-surface BCs (at $y = \pm L_0$). We drive the migration of a $\Sigma 37$ GB with a chemical potential jump driving force at different temperatures and allow for all of the disconnection modes shown in Figure 2(c) where the activation energies for disconnection nucleations are as shown in Fig. 2(a). Figure 7(a)

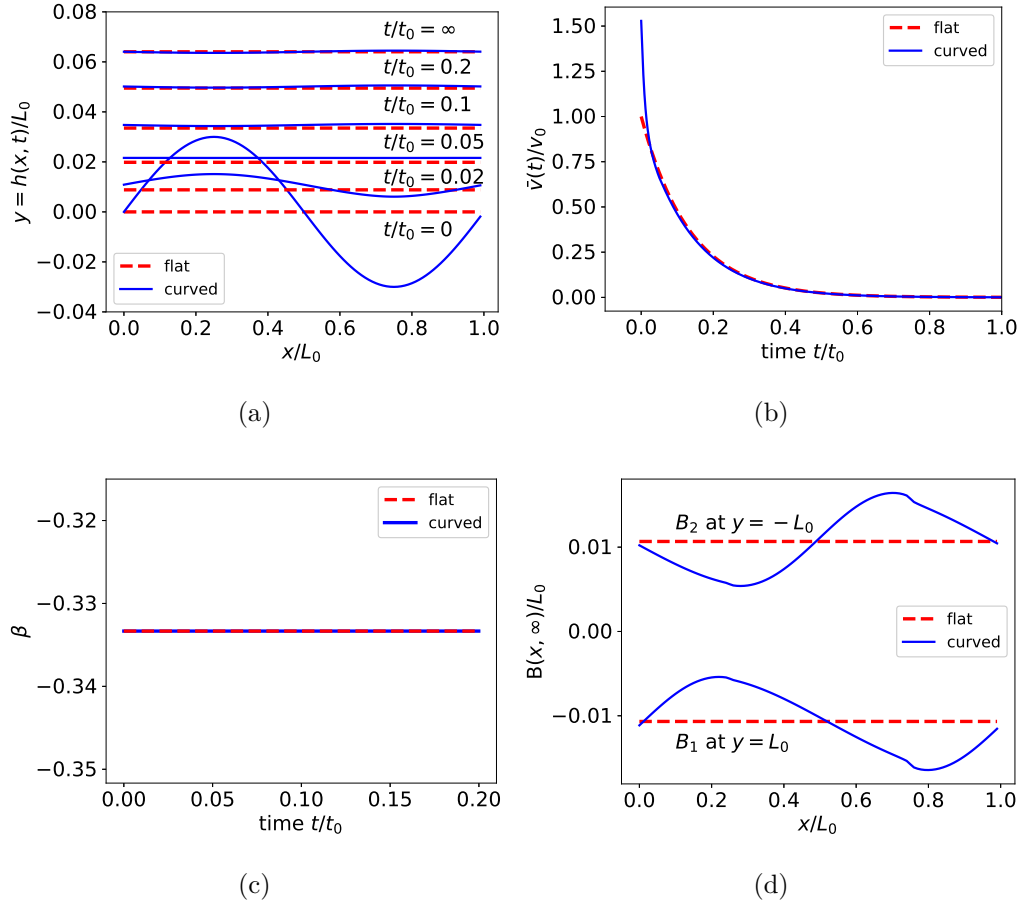


Figure 6: Single-mode migration of a $\Sigma 37$ GB with fixed-surface BCs at the top and bottom boundaries ($y = \pm L_0$). (a) The migration of a flat and curved GB under a chemical potential jump driving force $\Psi = -1 \text{ meV}/\text{\AA}^3$. The GBs migrate a short distance and then stagnate. (b) The average GB velocities $\bar{v}(t)$ of the flat and curved GBs. (c) The coupling factor of the flat and curved GBs during migration. (d) The coupled shear deformation at the top and bottom surfaces $B(x, t = \infty)$ (see Eq. 15) when GB migration stagnates.

shows that GB migration effectively stagnates at low temperature $T = 600 \text{ K}$ (note this GB does migrate, albeit extremely slowly), but at higher temperatures it migrates at a constant velocity (following an initial transient) that increases with increasing temperature (see Fig. 7(b)). These observations may be interpreted as follows. When the temperature is small, only one disconnection mode is activated and GB motion will stagnate, as shown in Fig. 6. With increasing temperature, the generation of disconnections of higher modes are thermally activated. Some of these higher modes have β with the opposite sign of the primary mode, allowing GB migration in the same direction as from the primary mode but with lateral translation in the

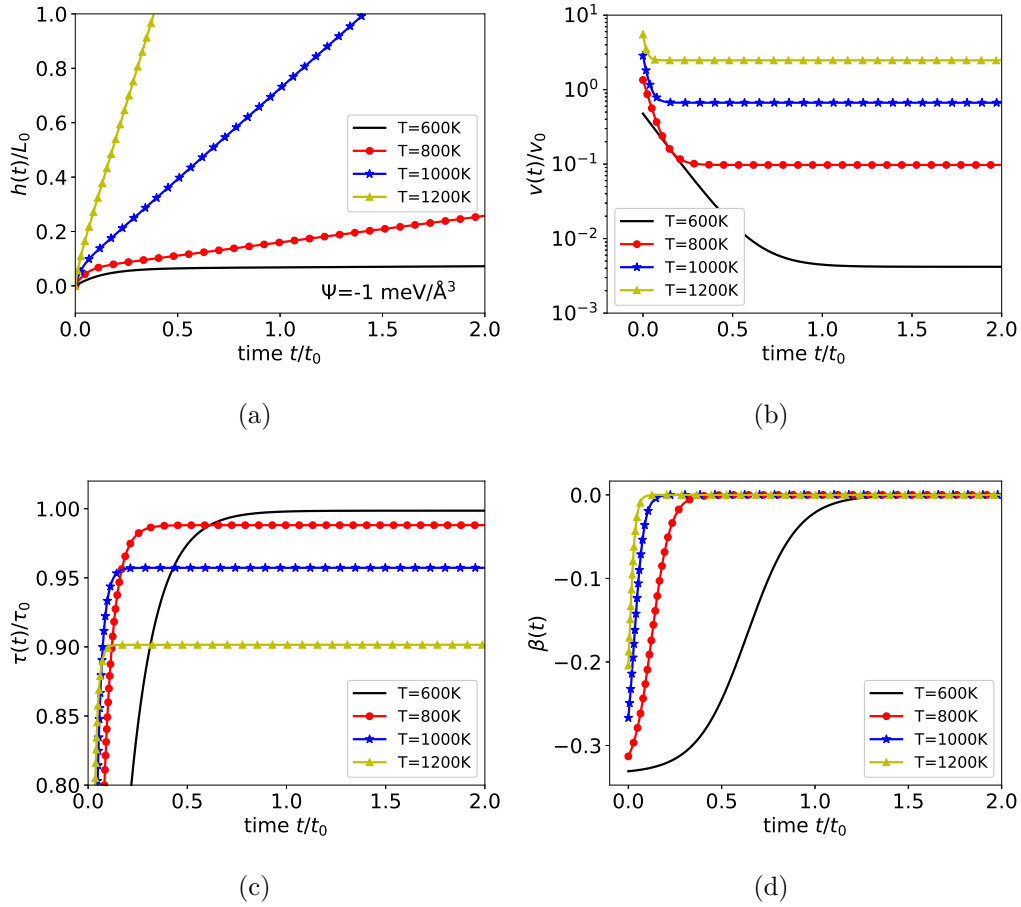


Figure 7: Multi-mode migration of the $\Sigma 37$ GB under fixed-surface boundary condition as a function of temperatures. (a) The GB position $h(t)/L_0$ as a function of time for $T = 600, 800, 1000, 1200$ K. The GB reaches the top boundary at $h/L_0 = 1$. (b) The GB migration velocity $v(t)/v_0$, where $v_0 = L_0/t_0$. Following an initial transient, the GB velocity approaches a temperature-dependent steady-state velocity. (c) The time dependence of the image shear stress $\tau(t)/\tau_0$ in the bicrystal (associated with the fixed-surface boundary conditions). Following an initial transient, the image stress approaches a temperature-dependent value such consistent with zero lateral grain translation. (d) The time dependence of the shear coupling factor $\beta(t)$. $\beta(0)$ is temperature-dependent and $\beta(t) \rightarrow 0$ at late time, where the rate of lateral grain translation tends to zero in steady-state GB migration.

opposite direction as the primary mode. This means that the motion of the disconnections of the primary mode shears the bicrystal in one direction and the secondary (and perhaps other) mode disconnections unshar the bicrystal. The Peach-Koehler force associated with the stress accumulated during GB migration ($\hat{\sigma}$) (arising from the fixed-surface BC during shear-coupled GB migration) opposes the motion of primary mode disconnections but enhances the motion of secondary (and other) mode disconnections. Migration under the action of these multiple

modes with fixed-surface BCs is balanced such that continuing GB migration creates no additional shear deformation.

In the present case (flat GBs with fixed-surface BCs), steady-state GB motion is achieved when the lateral translation rates of the two grains is zero, $\partial_t B = 0$. In steady-state, there may be a non-zero image stress $\hat{\sigma}$ in the bicrystal, that acts like an applied, external stress on the GB, as seen in Fig. 7(c). This steady-state stress is $\tau(t = \infty) = -\sum_i \Psi H_i b_i c_i / \sum_i b_i^2 c_i$ (for a flat GB driven by a chemical potential jump). When only one disconnection mode operates (as in Fig. 6), this steady-state stress $\tau_0 = -\Psi H_{10}/b_1$ gives rise to a Peach-Koehler force that cancels the chemical potential jump driving force and GB migration stagnates. When multiple disconnection modes are operating, GB migration achieves a constant velocity which decouples from the lateral grain translation; this implies that the shear-coupling factor $\beta(t) \rightarrow 0$ in Fig. 7(d), i.e., pure migration and no net shear coupling. While the MD simulations (Thomas et al., 2017) showed that the bicrystal alternately shears and unshears during GB migration, in the continuum limit no such alternating shearing and unshearing occurs since disconnection nucleation is continuous. The same approach can be applied to understand the initial ($t \rightarrow 0$) shear-coupling factor. The initial shear-coupling factor accounts for the nucleation and motion of disconnection of all modes, i.e., $\beta(t \rightarrow 0) = \sum_i (\tau_0 b_i + \Psi H_i) c_i b_i / \sum_i (\tau_0 b_i + \Psi H_i) c_i H_i$.

With free-surface BCs, a flat GB with multiple disconnection modes will migrate at a constant rate as it does in the single disconnection mode case, albeit with a different (temperature-dependent) velocity and with a different (temperature-dependent) shear-coupling factor that represent appropriate averages of all of the disconnection modes. The coupling factor is given by the same expression as for the initial coupling factor of GB migration under fixed-surface BCs.

The migration of curved (sinusoidal) GBs with multiple disconnection modes is influenced by both the effects of the BCs and the competition between different disconnection modes, as in the flat GB case. Moreover, the shear-coupled migration behavior of curved GBs also strongly depends on the initial distribution of density of disconnection of each mode. Unlike in the single-mode case, however, the relationship between GB shape and the densities of disconnections of different modes is not unique in the multi-mode case. In fact, for a GB of a given shape $h(x)$, there are infinitely many possible disconnection density distributions that satisfy the GB

shape constraint $\partial_x h = \sum_i \rho_i H_i$. In general, the disconnection density distribution is history-dependent. In the next section, we discuss the equilibrium disconnection density profile for GBs with pinned ends.

3.2. Evolution and Equilibrium of Grain Boundaries with Pinned Ends

Unlike in the ideal case of bicrystals, in polycrystals, GBs are of finite length (area) - inevitably delimited by the triple junctions and higher-order junctions at (along) which multiple grains/GBs meet. Not surprisingly, GB motion is affected by the resulting finite-size constraint and/or by the TJ dynamics. We now consider the effects of finite GB lengths (areas) on the evolution of GBs; in particular, we assume (for now) that the TJs are pinned. To this end, we first establish appropriate BCs at the two ends of a GB in Eqs. (1–2). Fixed ends imply that $\partial_t h(0, t) = \partial_t h(L_0, t) = 0$, where now L_0 is the distance between TJs. We also assume that no disconnection flows through the TJs, i.e., $J_i(0, t) = J_i(L_0, t) = 0$ for all disconnection modes i . We now examine the dynamics of such delimited GBs and their equilibrium profiles (i.e., GB shape and disconnection density distribution) for different types of driving forces. In all simulations, we assume that the initial GB is flat, $h(x, 0) = 0$, and there is zero net Burgers vector density $\rho_i(x, 0) = 0$ for all i .

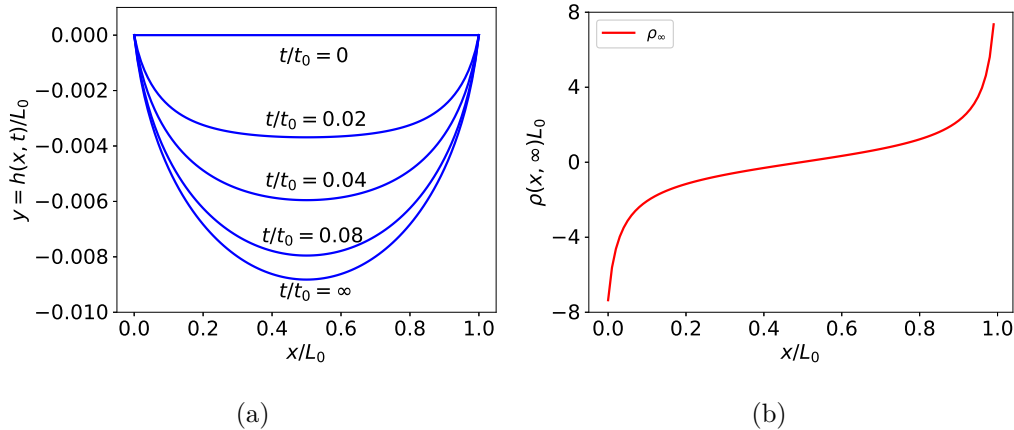


Figure 8: Single-mode GB migration of a $\Sigma 37$ GB with pinned ends under an applied stress. (a) The evolution of the $\Sigma 37$ GB driven by applied stress $\tau_0 = 5 \times 10^{-3} \mu$ at $T = 600$ K. (b) The disconnection density distribution in equilibrium, $\rho(x, t = \infty)$.

We first consider the GB migration of a $\Sigma 37$ GB with only a single disconnection mode under an applied shear stress $\tau_0/\mu = 5 \times 10^{-3}$, as shown in Fig. 8. The initially flat GB bows out and the

disconnections pile up near the two, pinned ends of the GB. At late time, the GB approaches a steady shape and the disconnection glide velocity goes to zero, $v_d = M_d[(\sigma + \tau_0)b - \gamma \partial_{xx} h H] = 0$. The GB shape profile (and the disconnection density distribution) may be implicitly determined from this expression. The GB profile evolution is the same whether the GB is driven by an applied stress (τ_0) or a jump in the chemical potential across the GB (Ψ) provided that $\Psi H = \tau_0 b$ (Zhang et al., 2017). However, when multiple disconnection modes are activated, the evolution depends on the nature of the driving forces.

We now examine the behavior based upon the multi-mode GB equation of motion. For a GB in equilibrium, the glide velocities of all disconnections must vanish, i.e., $v_i = M_d[(\sigma + \tau)b_i + (\Psi - \gamma \partial_{xx} h)H_i] = 0$ for all i . Since the shear-coupling factors $\beta_i = -b_i/H_i$ of different disconnection modes will, in general, be distinct, this implies that there must be zero driving force associated with both the disconnection Burgers vector ($f_b = 0$) and the GB step character ($f_h = 0$). Hence, in equilibrium, $\sigma = -\tau$ and $\Psi = \gamma \partial_{xx} h$. Moreover, since the two ends are pinned at $x/L_0 = 0$ and 1, the equilibrium GB shape is a parabola (independent of the applied stress τ), $h(x) = (\Psi/\gamma)(x^2 - x)$ for the case of an isotropic GB energy γ . Note that in most materials γ depends on GB crystallography (e.g., the GB inclination $\partial_x h$ and grain misorientation); in this case the equilibrium shape will not be a parabola but may be found from $\Psi = \gamma(\partial_x h)\partial_{xx} h$. We validate these predictions via simulations below.

We now consider the simple case in which only two disconnection modes with opposite shear-coupling factors (two-mode GB migration) are activated. In particular, consider the stress-driven motion of a $\Sigma 13$ GB in a face centered cubic material with the two lowest disconnection formation energy modes (and opposite shear coupling factors); i.e., $(a_0/\sqrt{26}, -5a_0/2\sqrt{26})$ and $(a_0/\sqrt{26}, 4a_0/\sqrt{26})$, where a_0 is the cubic lattice parameter. We observe two stages of evolution in Fig. 9(a): in the first stage, the GB bows out quickly (as in the single-mode case, Fig. 8) followed by a second stage in which the GB slowly flattens/retracts, eventually returning to its initially flat shape. From the observation of the stresses $\sigma(x, t)$ from the disconnections along the GB Fig. 9(b), we find that during the first stage, disconnections glide along the GB mainly driven by the external applied stress and rapidly reach a state such that the internal stress *nearly* offsets the external applied stress, i.e., $\sigma(t) \approx -\tau_0$. In the second stage, the GB migration is mainly driven by the capillary force (i.e., the $\partial_{xx} h$ term). Although the GB eventually returns

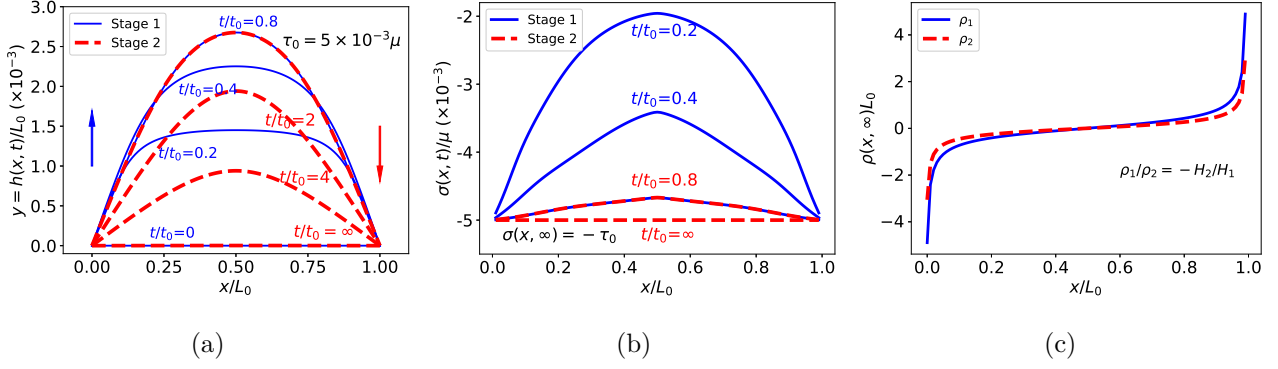


Figure 9: Two-mode migration of the $\Sigma 13$ GB with pinned ends under an applied stress $\tau_0/\mu = 5 \times 10^{-3}$ at $T = 800$ K. (a) The evolution of this GB; the GB bows out at early time (stage 1, $t/t_0 < 0.8$) and then retracts back (stage 2, $t/t_0 > 0.8$). Arrows indicate the GB migration directions during the two stages. (b) The internal shear stress from all of the disconnections $\sigma(x, t)$. At equilibrium, the internal stress balances the external applied stress, i.e., $\sigma(x, \infty) = -\tau_0$. (c) The disconnection density distribution at equilibrium ($\rho_1(x, \infty)H_1 + \rho_2(x, \infty)H_2 = 0$).

to a flat shape, the equilibrium distributions of the disconnection densities are nonzero along the GB and satisfy the zero net step condition $\rho_1 H_1 + \rho_2 H_2 = 0$ (as determined by $\partial_{xx} h = 0$) while the net Burgers vector density $\rho_1 b_1 + \rho_2 b_2 \neq 0$ (as determined by $\sigma = -\tau_0$), as illustrated in Fig. 9(c).

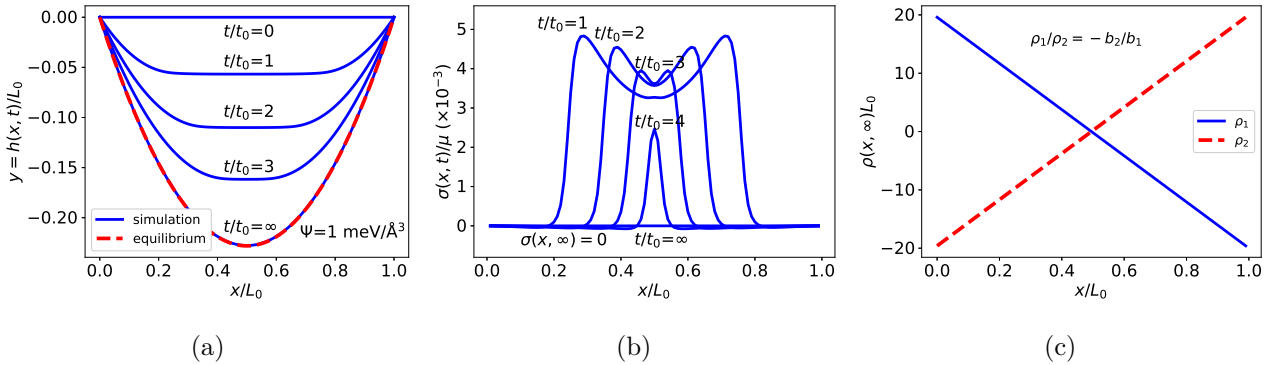


Figure 10: Two-mode migration of the $\Sigma 13$ GB with pinned ends driven by a jump in chemical potential. (a) The evolution of the $\Sigma 13$ GB driven with $\Psi = 1 \text{ meV}/\text{\AA}^3$ at $T = 800$ K. (b) The internal shear stress associated with the disconnections $\sigma(x, t)$. At equilibrium, the internal stress vanishes, i.e., $\sigma(x, t = \infty) = 0$. (c) The equilibrium disconnection density distributions: $\rho_1(x, \infty)b_1 + \rho_2(x, \infty)b_2 = 0$ implying that there is zero net Burgers vector along GB.

Next, we drive the same two disconnection mode GB with a jump in chemical potential (and zero applied stress). As shown in Fig. 10(a), the GB bows out from its flat initial state, attaining a stationary profile at late time that is parabolic in agreement with our theoretical prediction. In this equilibrium state, the stress along the GB $\sigma = 0$ (see Fig. 10(b)) and the capillarity driving force balances the chemical potential jump ($\gamma\partial_{xx}h = \Psi$). The corresponding equilibrium disconnection density satisfy the conditions $\rho_1b_1 + \rho_2b_2 = 0$ and $\rho_1H_1 + \rho_2H_2 = \partial_xh = (\Psi/\gamma)(2x - 1)$; see Fig. 10(c).

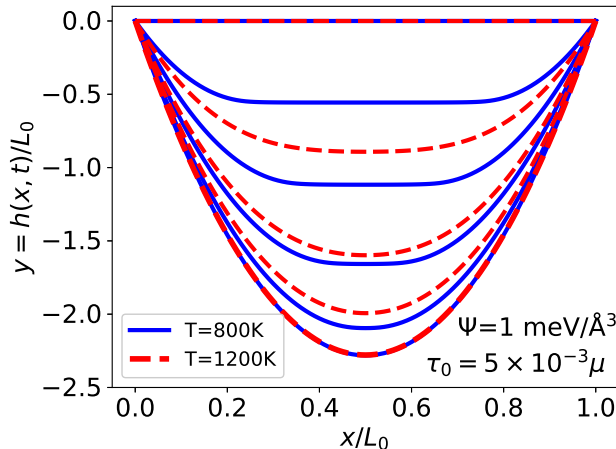


Figure 11: Multi-mode migration of a $\Sigma 13$ GB with pinned ends at $T = 800$ K and 1200 K under mixed driving forces; i.e., $\tau_0/\mu = 5 \times 10^{-3}$ and $\Psi = 1 \text{ meV}/\text{\AA}^3$. Solid lines represent the GB evolution at $T = 800$ K at $t/t_0 = 1, 2, 3, \infty$; dashed lines represent the GB evolution at $T = 1200$ K at $t/t_0 = 0.1, 0.2, 0.3, \infty$.

As a general example of multi-mode GB migration, we examine the $\Sigma 13$ GB with all disconnection modes; see Fig. 2. Figure 11 shows the evolution of the GB under mixed driving forces, simultaneously including an applied stress and synthetic force at $T = 800$ K and 1200 K. The GB migrates to the same parabolic equilibrium shape at both temperatures, but with a much faster velocity at higher temperature. The results indicate that the multi-mode GB migration is similar to the two-mode GB migration example in Figs. 9 and 10 (despite the difference in the equilibrium disconnection density distribution), but is very distinct from the single-mode GB migration results (Fig. 8).

While all disconnection modes may play a role in GB migration and sliding, the importance of the different disconnection modes depend on their relative ease of nucleation (nucleation barrier, heterogeneous sites, interactions with lattice defects), which varies between GBs of different

bicystallography and atomic bonding, and the nature of the driving force. This implies that different GBs will behave differently during the evolution of polycrystalline microstructures and these differences will be a function of temperature. The present results also demonstrate that grain size also matters; triple junction effects will be much more important in nanocrystalline materials where each grain boundary length (area) is small, as compared with large grained materials.

4. SUMMARY AND DISCUSSION

Discrete models of grain boundary migration based upon disconnection motion have previously been proposed (e.g., see (Han et al., 2018)) and have enjoyed considerable success. However, if our goal is to describe GB migration in a microstructure, tracking discrete disconnections throughout the entire microstructure is not practical. The main goal of this study has been the development of a continuum model of GB dynamics that respects the underlying microscopic mechanisms of GB migration (i.e., disconnection motion) without the excessive computational demands of tracking every disconnection.

We presented such a continuum model for grain boundary dynamics (including migration and shear) based upon multiple disconnection modes which is a generalization of an earlier single disconnection mode model (Zhang et al., 2017). In this model, GBs migrate via the thermally-activated nucleation and motion of disconnections of different modes along the GBs. The key to the temperature-dependence of GB dynamics is the competition and/or synergies of the different disconnection modes. Grain boundary migration is, in general, coupled to shear deformation through disconnection motion, although different disconnection modes may conspire to decouple these. We implement our model in continuum numerical simulations for GB dynamics in single and multi-mode disconnection limits in both a bicrystal (under two types of boundary conditions) and for a finite-length GB with pinned ends. The simulation results demonstrate that the selection of and competition between different disconnection modes lead to complex and diverse shear-coupled GB migration behavior (and hence grain growth) in a polycrystalline material. When the shear deformation is constrained by fixed-surface BCs, as a model for a GB in a polycrystal, shear-coupling implies stress generation that can lead to GB stagnation at low temperature, where only a single disconnection mode is active. This

constraint and the concomitant stress generation may be accommodated by the cooperation of multiple disconnection modes at high temperature such that GB motion can occur without shear-coupling. The temperature at which this transition in behavior occurs varies between GBs, depending on their relative disconnection nucleation barrier spectrum.

Our simulations provide clear demonstrations of the importance of including a crystallography-respecting, microscopic model for microstructure evolution and the intrinsic coupling between stress, capillarity, and microstructure geometry in microstructure evolution. Unlike in conventional description of GB motion and grain growth, the GB mobility and shear coupling are not intrinsic properties of a GB but rather depend on the properties of their disconnections as well as how the GB is driven, microstructure geometry, and boundary conditions (Chen et al., 2019).

The relative importance of different disconnection modes should, in general, depend on the relative ease of their nucleation and motion; these are functions of temperature and atomic-scale structure of the GBs. The present model only considers GB motion controlled by disconnection nucleation; this implicitly assumes that disconnection motion is fast compared with disconnection migration (an assumption that is not always justified (Combe et al., 2016)). Further, the model for disconnection nucleation (Han et al., 2018) is based upon a model which may be oversimplified. This implies that the prediction of GB dynamics based upon the disconnection model requires more detailed and accurate models for disconnection nucleation and migration barriers that provide more rigorous descriptions of GB structure, disconnection core structure and bonding. Such input may be obtained from atomistic simulations that provide these barriers (e.g., using a transition barrier finding approach such as the nudged elastic band method (Combe et al., 2016)) and, ideally, incorporate accurate descriptions of atomic interactions (based upon first-principles methods).

Modeling the evolution of a polycrystalline microstructure requires a description of the spatial distribution of triple junctions, the topology of the microstructure, and grain size, as well as a description of how TJs move. In this paper, we considered only stationary (immobile) TJs, that serve as fixed GB termini. The disconnection description of GB dynamics has the potential to describe many of the complexities of microstructure evolution, including TJ dynamics (Han et al., 2018; Zhang et al., 2017). Just as disconnection dynamics provides a robust approach for describing GB dynamics, we expect that it can also be extended to understand TJ

motion, as recently proposed by Thomas et al. (2019).

While a disconnection model for shear-coupled grain boundary migration is a promising approach for describing microstructure evolution, a number of important opportunities remain. Although the present disconnection model of GB migration implicitly links microstructure evolution and mechanics, a more complete integration would couple grain boundary migration, grain boundary sliding, grain rotation and stress generation. This, together with better descriptions of disconnection dynamics at triple junctions and the dynamics of GBs of arbitrary inclination/shape, can be used to develop predictive models for microstructure evolution. Further, since the Hall-Petch effect (grain size strengthening) is based on GBs blocking lattice dislocations, a more complete understanding of how GBs block, absorb, and transmit dislocation is important for describing plasticity in polycrystals. Such effects are controlled, in part, by disconnection activity in the GB. An extension of the present work to develop a crystallography-sensitive continuum model could be used to augment crystal plasticity descriptions of deformation to make such models microstructure-sensitive. While GBs can absorb point defects (e.g., in radiation damage scenarios), some GBs readily absorb point defects while others do not. This implies a connection between GB dynamics and point defect absorption efficiency. A continuum disconnection-based model could couple GB adsorption efficiency, GB crystallography, and microstructure evolution. This short list suggests that the coupling of microstructure evolution, defect dynamics within grains, and deformation within a disconnection-based, crystallography-respecting continuum description is a promising direction for both materials science and the mechanics of materials.

Acknowledgement

The research contributions of D.J.S and J.H were sponsored by the Army Research Office and were accomplished under Grant Number W911NF-19-1-0263. The views and conclusions contained in this document are those of the authors and should not be interpreted as representing the official policies, either expressed or implied, of the Army Research Office or the U.S. Government. The U.S. Government is authorized to reproduce and distribute reprints for Government purposes notwithstanding any copyright notation herein. Y.X. acknowledges support from the Hong Kong Research Grants Council General Research Fund 16302818.

Appendix A. Elasticity solutions

The stress and displacement fields for a period array of dislocations (periodicity $2w$) are given in Hirth and Lothe (1982) and Van der Giessen and Needleman (1995)

$$\begin{aligned}
\sigma_{11} &= -\frac{\mu b}{4w(1-\nu)} \frac{1}{\cosh(\pi\eta) - \cos(\pi\xi)} \left[2 \sinh(\pi\eta) + \pi\eta \frac{1 - \cos(\pi\xi) \cosh(\pi\eta)}{\cosh(\pi\eta) - \cos(\pi\xi)} \right], \\
\sigma_{22} &= \frac{\mu b}{4w(1-\nu)} \left[\pi\eta \frac{1 - \cos(\pi\xi) \cosh(\pi\eta)}{(\cosh(\pi\eta) - \cos(\pi\xi))^2} \right], \\
\sigma_{12} &= \frac{\mu b}{4w(1-\nu)} \frac{\sin(\pi\xi)}{\cosh(\pi\eta) - \cos(\pi\xi)} \left[1 - \pi\eta \frac{\sinh(\pi\eta)}{\cosh(\pi\eta) - \cos(\pi\xi)} \right], \\
u_1(x, y) &= \frac{b}{2\pi(1-\nu)} \left[\frac{1}{4} \frac{\pi\eta \sin(\pi\xi)}{\cosh(\pi\eta) - \cos(\pi\xi)} - (1-\nu) \tan^{-1} \left(\frac{\tan(\pi\xi/2)}{\tanh(\pi\eta/2)} \right) \right], \\
u_2(x, y) &= \frac{b}{2\pi(1-\nu)} \left[\frac{1}{4} \frac{\pi\eta \sinh(\pi\eta)}{\cosh(\pi\eta) - \cos(\pi\xi)} - \frac{1}{4} (1-2\nu) \ln \left(\cosh(\pi\eta) - \cos(\pi\xi) \right) \right],
\end{aligned} \tag{A.1}$$

where

$$\xi = \frac{x - x_0}{w}, \quad \eta = \frac{y - y_0}{w}. \tag{A.2}$$

A Fourier series description of the Airy stress function for free-surface boundary condition is as follows:

$$\begin{aligned}
\varphi(x, y) &= \sum_k \hat{\varphi} e^{ikx}, \\
\hat{\varphi}(k, y) &= (A_1 + B_1 y) \cosh(ky) + (A_2 + B_2 y) \sinh(ky), \\
A_1 &= -\frac{1}{\cosh(kL_y)} \left(\frac{\hat{g}_1 + \hat{g}_2}{2k^2} + \frac{L_y}{k} \Psi_2 \right), \quad B_1 = \frac{1}{k \cosh(kL_y)} \Psi_1, \\
A_2 &= -\frac{1}{\sinh(kL_y)} \left(\frac{\hat{g}_1 - \hat{g}_2}{2k^2} + \frac{L_y}{k} \Psi_1 \right), \quad B_2 = \frac{1}{k \cosh(kL_y)} \Psi_2, \\
\Psi_1 &= \frac{i \tanh(kL_y) (\hat{f}_1 + \hat{f}_2) + (\hat{g}_1 - \hat{g}_2)}{2kL_y (\tanh^2(kL_y) - 1) + 2 \tanh(kL_y)}, \\
\Psi_2 &= \frac{i (\hat{f}_1 - \hat{f}_2) + \tanh(kL_y) (\hat{g}_1 + \hat{g}_2)}{2kL_y (1 - \tanh^2(kL_y)) + 2 \tanh(kL_y)},
\end{aligned} \tag{A.3}$$

where \hat{f}_i and \hat{g}_i are Fourier coefficients of f_i and g_i for $i = 1, 2$, respectively. We can easily apply this stress function to obtain the stress field in the usual manner as

$$\sigma_{11} = \frac{\partial^2 \varphi}{\partial y^2}, \quad \sigma_{12} = -\frac{\partial^2 \varphi}{\partial x \partial y}, \quad \sigma_{22} = \frac{\partial^2 \varphi}{\partial x^2}. \tag{A.4}$$

The Fourier coefficients of the displacement field for fixed-surface boundary condition

$$\begin{aligned}\hat{u}_1(k, y) &= (A_1 + B_1 y) \cosh(ky) + (C_1 + D_1 y) \sinh(ky), \\ \hat{u}_2(k, y) &= (A_2 + B_2 y) \cosh(ky) + (C_2 + D_2 y) \sinh(ky),\end{aligned}\tag{A.5}$$

where the coefficients are

$$\begin{aligned}A_1 &= i \left[C_2 + \frac{3 - 4\nu}{k} B_2 \right], \quad B_1 = i D_2, \\ C_1 &= i \left[A_2 + \frac{3 - 4\nu}{k} D_2 \right], \quad D_1 = i B_2, \\ A_2 &= \frac{\hat{g}_1 + \hat{g}_2}{2 \cosh(kL_y)} - L_y \tanh(kL_y) D_2, \quad B_2 = \frac{k}{\cosh(kL_y)} \Psi_1, \\ C_2 &= \frac{\hat{g}_1 - \hat{g}_2}{2 \sinh(kL_y)} - L_y \coth(kL_y) B_2, \quad D_2 = \frac{-k}{\cosh(kL_y)} \Psi_2, \\ \Psi_1 &= \frac{i \tanh(kL_y) (\hat{f}_1 + \hat{f}_2) + (\hat{g}_1 - \hat{g}_2)}{2kL_y (1 - \tanh^2(kL_y)) - 2(3 - 4\nu) \tanh(kL_y)} \operatorname{sgn}(\eta), \\ \Psi_2 &= \frac{i(\hat{f}_1 - \hat{f}_2) + \tanh(kL_y) (\hat{g}_1 + \hat{g}_2)}{2kL_y (1 - \tanh^2(kL_y)) + 2(3 - 4\nu) \tanh(kL_y)}.\end{aligned}\tag{A.6}$$

Ashby, M., 1972. Boundary defects, and atomistic aspects of boundary sliding and diffusional creep. *Surface Science* 31, 498 – 542. URL: <http://www.sciencedirect.com/science/article/pii/0039602872902737>, doi:[https://doi.org/10.1016/0039-6028\(72\)90273-7](https://doi.org/10.1016/0039-6028(72)90273-7).

Bainbridge, D.W., Choh, H.L., Edwards, E.H., 1954. Recent observations on the motion of small angle dislocation boundaries. *Acta Metallurgica* 2, 322 – 333. URL: <http://www.sciencedirect.com/science/article/pii/0001616054901753>, doi:[https://doi.org/10.1016/0001-6160\(54\)90175-3](https://doi.org/10.1016/0001-6160(54)90175-3).

Bollmann, W., 1970. *Crystal Defects and Crystalline Interfaces*. Springer Berlin Heidelberg. URL: <https://books.google.com.hk/books?id=i4TZRgAACAAJ>.

Cahn, J.W., Mishin, Y., Suzuki, A., 2006. Coupling grain boundary motion to shear deformation. *Acta Materialia* 54, 4953 – 4975. URL: <http://www.sciencedirect.com/science/article/pii/S1359645406005313>, doi:<https://doi.org/10.1016/j.actamat.2006.08.004>.

- Cahn, J.W., Taylor, J.E., 2004. A unified approach to motion of grain boundaries, relative tangential translation along grain boundaries, and grain rotation. *Acta Materialia* 52, 4887 – 4898. URL: <http://www.sciencedirect.com/science/article/pii/S1359645404003945>, doi:<https://doi.org/10.1016/j.actamat.2004.02.048>.
- Chen, K., Han, J., Thomas, S.L., Srolovitz, D.J., 2019. Grain boundary shear coupling is not a grain boundary property. *Acta Materialia* 167, 241 – 247. URL: <http://www.sciencedirect.com/science/article/pii/S1359645419300552>, doi:<https://doi.org/10.1016/j.actamat.2019.01.040>.
- Chen, L.Q., Kalonji, G., 1992. Finite temperature structure and properties of $\theta = 5$ (310) tilt grain boundaries in nacl a molecular dynamics study. *Philosophical Magazine A* 66, 11–26. URL: <https://doi.org/10.1080/01418619208201510>, doi:10.1080/01418619208201510, arXiv:<https://doi.org/10.1080/01418619208201510>.
- Chen, L.Q., Yang, W., 1994. Computer simulation of the domain dynamics of a quenched system with a large number of nonconserved order parameters: The grain-growth kinetics. *Physical Review B* 50, 15752–15756. URL: <https://link.aps.org/doi/10.1103/PhysRevB.50.15752>, doi:10.1103/PhysRevB.50.15752.
- Combe, N., Momprou, F., Legros, M., 2016. Disconnections kinks and competing modes in shear-coupled grain boundary migration. *Phys. Rev. B* 93, 024109. URL: <https://link.aps.org/doi/10.1103/PhysRevB.93.024109>, doi:10.1103/PhysRevB.93.024109.
- DeCost, B.L., Holm, E.A., 2017. Phenomenology of Abnormal Grain Growth in Systems with Nonuniform Grain Boundary Mobility. *Metallurgical and Materials Transactions A* 48, 2771–2780. doi:10.1007/s11661-016-3673-6.
- Elsay, M., Esedođlu, S., Smereka, P., 2009. Diffusion generated motion for grain growth in two and three dimensions. *Journal of Computational Physics* 228, 8015 – 8033. URL: <http://www.sciencedirect.com/science/article/pii/S0021999109004082>, doi:<https://doi.org/10.1016/j.jcp.2009.07.020>.

- Esedoglu, S., 2016. Grain size distribution under simultaneous grain boundary migration and grain rotation in two dimensions. *Computational Materials Science* 121, 209–216.
- Van der Giessen, E., Needleman, A., 1995. Discrete dislocation plasticity: a simple planar model. *Modelling and Simulation in Materials Science and Engineering* 3, 689. URL: <http://stacks.iop.org/0965-0393/3/i=5/a=008>.
- Gottstein, G., Molodov, D., Shvindlerman, L., Srolovitz, D., Winning, M., 2001. Grain boundary migration: misorientation dependence. *Current Opinion in Solid State and Materials Science* 5, 9 – 14. URL: <http://www.sciencedirect.com/science/article/pii/S1359028600000309>, doi:[https://doi.org/10.1016/S1359-0286\(00\)00030-9](https://doi.org/10.1016/S1359-0286(00)00030-9).
- Hamilton, J.C., Foiles, S.M., 2002. First-principles calculations of grain boundary theoretical shear strength using transition state finding to determine generalized gamma surface cross sections. *Physical Review B* 65, 064104. URL: <https://link.aps.org/doi/10.1103/PhysRevB.65.064104>, doi:[10.1103/PhysRevB.65.064104](https://doi.org/10.1103/PhysRevB.65.064104).
- Han, J., Thomas, S.L., Srolovitz, D.J., 2018. Grain-boundary kinetics: A unified approach. *Progress in Materials Science* , –URL: <https://www.sciencedirect.com/science/article/pii/S0079642518300641>, doi:<https://doi.org/10.1016/j.pmatsci.2018.05.004>.
- Han, J., Vitek, V., Srolovitz, D.J., 2017. The grain-boundary structural unit model redux. *Acta Materialia* 133, 186 – 199. URL: <http://www.sciencedirect.com/science/article/pii/S1359645417303798>, doi:<https://doi.org/10.1016/j.actamat.2017.05.002>.
- Harris, K., Singh, V., King, A., 1998. Grain rotation in thin films of gold. *Acta Materialia* 46, 2623 – 2633. URL: <http://www.sciencedirect.com/science/article/pii/S1359645497004679>, doi:[https://doi.org/10.1016/S1359-6454\(97\)00467-9](https://doi.org/10.1016/S1359-6454(97)00467-9).

- Hillert, M., 1965. On the theory of normal and abnormal grain growth. *Acta Metallurgica* 13, 227 – 238. URL: <http://www.sciencedirect.com/science/article/pii/0001616065902002>, doi:[https://doi.org/10.1016/0001-6160\(65\)90200-2](https://doi.org/10.1016/0001-6160(65)90200-2).
- Hirth, J., Pond, R., 1996. Steps, dislocations and disconnections as interface defects relating to structure and phase transformations. *Acta Materialia* 44, 4749 – 4763. URL: <http://www.sciencedirect.com/science/article/pii/S1359645496001322>, doi:[https://doi.org/10.1016/S1359-6454\(96\)00132-2](https://doi.org/10.1016/S1359-6454(96)00132-2).
- Hirth, J.P., Lothe, J., 1982. *Theory of dislocations*. 2nd ed ed., New York: Wiley.
- Homer, E.R., Foiles, S.M., Holm, E.A., Olmsted, D.L., 2013. Phenomenology of shear-coupled grain boundary motion in symmetric tilt and general grain boundaries. *Acta Materialia* 61, 1048 – 1060. URL: <http://www.sciencedirect.com/science/article/pii/S1359645412007306>, doi:<https://doi.org/10.1016/j.actamat.2012.10.005>.
- Janssens, K.G., Olmsted, D., Holm, E.A., Foiles, S.M., Plimpton, S.J., Derlet, P.M., 2006. Computing the mobility of grain boundaries. *Nature materials* 5, 124.
- Jin, M., Minor, A., Stach, E., Morris, J., 2004. Direct observation of deformation-induced grain growth during the nanoindentation of ultrafine-grained al at room temperature. *Acta Materialia* 52, 5381 – 5387. URL: <http://www.sciencedirect.com/science/article/pii/S1359645404004653>, doi:<https://doi.org/10.1016/j.actamat.2004.07.044>.
- Kazaryan, A., Wang, Y., Dregia, S.A., Patton, B.R., 2000. Generalized phase-field model for computer simulation of grain growth in anisotropic systems. *Physical Review B* 61, 14275–14278. URL: <https://link.aps.org/doi/10.1103/PhysRevB.61.14275>, doi:[10.1103/PhysRevB.61.14275](https://doi.org/10.1103/PhysRevB.61.14275).
- Kinderlehrer, D., Livshits, I., Taasan, S., 2006. A variational approach to modeling and simulation of grain growth. *SIAM Journal on Scientific Computing*

- 28, 1694–1715. URL: <https://doi.org/10.1137/030601971>, doi:10.1137/030601971, arXiv:<https://doi.org/10.1137/030601971>.
- King, A.H., Smith, D.A., 1980. The effects on grain-boundary processes of the steps in the boundary plane associated with the cores of grain-boundary dislocations. *Acta Crystallographica Section A* 36, 335–343. URL: <https://doi.org/10.1107/S0567739480000782>, doi:10.1107/S0567739480000782.
- Kobayashi, R., Warren, J.A., Carter, W.C., 2000. A continuum model of grain boundaries. *Physica D: Nonlinear Phenomena* 140, 141 – 150. URL: <http://www.sciencedirect.com/science/article/pii/S0167278900000233>, doi:[https://doi.org/10.1016/S0167-2789\(00\)00023-3](https://doi.org/10.1016/S0167-2789(00)00023-3).
- Lazar, E.A., MacPherson, R.D., Srolovitz, D.J., 2010. A more accurate two-dimensional grain growth algorithm. *Acta Materialia* 58, 364 – 372. URL: <http://www.sciencedirect.com/science/article/pii/S135964540900603X>, doi:<https://doi.org/10.1016/j.actamat.2009.09.008>.
- Legros, M., Gianola, D.S., Hemker, K.J., 2008. In situ tem observations of fast grain-boundary motion in stressed nanocrystalline aluminum films. *Acta Materialia* 56, 3380 – 3393. URL: <http://www.sciencedirect.com/science/article/pii/S1359645408002152>, doi:<https://doi.org/10.1016/j.actamat.2008.03.032>.
- LeSar, R., Najafabadi, R., Srolovitz, D.J., 1989. Finite-temperature defect properties from free-energy minimization. *Physical Review Letter* 63, 624–627. URL: <https://link.aps.org/doi/10.1103/PhysRevLett.63.624>, doi:10.1103/PhysRevLett.63.624.
- Li, C.H., Edwards, E., Washburn, J., Parker, E., 1953. Stress-induced movement of crystal boundaries. *Acta Metallurgica* 1, 223 – 229. URL: <http://www.sciencedirect.com/science/article/pii/0001616053900625>, doi:[https://doi.org/10.1016/0001-6160\(53\)90062-5](https://doi.org/10.1016/0001-6160(53)90062-5).

- Ma, E., 2004. Watching the nanograins roll. *Science* 305, 623–624. URL: <http://science.sciencemag.org/content/305/5684/623>, doi:10.1126/science.1101589, arXiv:<http://science.sciencemag.org/content/305/5684/623>.fu
- MacPherson, R.D., Srolovitz, D.J., 2007. The von neumann relation generalized to coarsening of three-dimensional microstructures. *Nature* 446, 1053.
- Mishin, Y., Mehl, M.J., Papaconstantopoulos, D.A., Voter, A.F., Kress, J.D., 2001. Structural stability and lattice defects in copper: Ab initio, tight-binding, and embedded-atom calculations. *Phys. Rev. B* 63, 224106. URL: <https://link.aps.org/doi/10.1103/PhysRevB.63.224106>, doi:10.1103/PhysRevB.63.224106.
- Molteni, C., Francis, G.P., Payne, M.C., Heine, V., 1996. First principles simulation of grain boundary sliding. *Physical Review Letter* 76, 1284–1287. URL: <https://link.aps.org/doi/10.1103/PhysRevLett.76.1284>, doi:10.1103/PhysRevLett.76.1284.
- Molteni, C., Marzari, N., Payne, M.C., Heine, V., 1997. Sliding mechanisms in aluminum grain boundaries. *Physical Review Letter* 79, 869–872. URL: <https://link.aps.org/doi/10.1103/PhysRevLett.79.869>, doi:10.1103/PhysRevLett.79.869.
- Mompiou, F., Legros, M., Ensslen, C., Kraft, O., 2015. In situ tem study of twin boundary migration in sub-micron be fibers. *Acta Materialia* 96, 57 – 65. URL: <http://www.sciencedirect.com/science/article/pii/S1359645415003997>, doi:<https://doi.org/10.1016/j.actamat.2015.06.016>.
- Mullins, W.W., 1956. Two-dimensional motion of idealized grain boundaries. *Journal of Applied Physics* 27, 900–904. URL: <https://doi.org/10.1063/1.1722511>, doi:10.1063/1.1722511, arXiv:<https://doi.org/10.1063/1.1722511>.
- Peach, M., Koehler, J.S., 1950. The forces exerted on dislocations and

- the stress fields produced by them. *Phys. Rev.* 80, 436–439. URL: <https://link.aps.org/doi/10.1103/PhysRev.80.436>, doi:10.1103/PhysRev.80.436.
- Rajabzadeh, A., Legros, M., Combe, N., Momprou, F., Molodov, D., 2013a. Evidence of grain boundary dislocation step motion associated to shear-coupled grain boundary migration. *Philosophical Magazine* 93, 1299–1316. URL: <https://doi.org/10.1080/14786435.2012.760760>, doi:10.1080/14786435.2012.760760, arXiv:<https://doi.org/10.1080/14786435.2012.760760>.
- Rajabzadeh, A., Momprou, F., Legros, M., Combe, N., 2013b. Elementary mechanisms of shear-coupled grain boundary migration. *Physical Review Letter* 110, 265507. URL: <https://link.aps.org/doi/10.1103/PhysRevLett.110.265507>, doi:10.1103/PhysRevLett.110.265507.
- Read, W.T., Shockley, W., 1950. Dislocation models of crystal grain boundaries. *Phys. Rev.* 78, 275–289. URL: <https://link.aps.org/doi/10.1103/PhysRev.78.275>, doi:10.1103/PhysRev.78.275.
- Riontino, G., Antonione, C., Battezzati, L., Marino, F., Tabasso, M.C., 1979. Kinetics of abnormal grain growth in pure iron. *Journal of Materials Science* 14, 86–90. URL: <https://doi.org/10.1007/BF01028331>, doi:10.1007/BF01028331.
- Rollett, A., Srolovitz, D., Anderson, M., 1989. Simulation and theory of abnormal grain growth–anisotropic grain boundary energies and mobilities. *Acta Metallurgica* 37, 1227 – 1240. URL: <http://www.sciencedirect.com/science/article/pii/000161608990117X>, doi:[https://doi.org/10.1016/0001-6160\(89\)90117-X](https://doi.org/10.1016/0001-6160(89)90117-X).
- Rupert, T.J., Gianola, D.S., Gan, Y., Hemker, K.J., 2009. Experimental observations of stress-driven grain boundary migration. *Science* 326, 1686–1690. URL: <http://science.sciencemag.org/content/326/5960/1686>, doi:10.1126/science.1178226, arXiv:<http://science.sciencemag.org/content/326/5960/1686.f>
- Sansoz, F., Molinari, J., 2005. Mechanical behavior of tilt grain boundaries in nanoscale cu and al: A quasicontinuum study. *Acta Materialia* 53, 1931 –

1944. URL: <http://www.sciencedirect.com/science/article/pii/S1359645405000182>, doi:<https://doi.org/10.1016/j.actamat.2005.01.007>.
- Schäfer, J., Albe, K., 2012. Competing deformation mechanisms in nanocrystalline metals and alloys: Coupled motion versus grain boundary sliding. *Acta Materialia* 60, 6076 – 6085. URL: <http://www.sciencedirect.com/science/article/pii/S1359645412004922>, doi:<https://doi.org/10.1016/j.actamat.2012.07.044>.
- Shan, Z., Stach, E.A., Wiezorek, J.M.K., Knapp, J.A., Follstaedt, D.M., Mao, S.X., 2004. Grain boundary-mediated plasticity in nanocrystalline nickel. *Science* 305, 654–657. URL: <http://science.sciencemag.org/content/305/5684/654>, doi:10.1126/science.1098741, arXiv:<http://science.sciencemag.org/content/305/5684/654>.fu
- Shiga, M., Shinoda, W., 2004. Stress-assisted grain boundary sliding and migration at finite temperature: A molecular dynamics study. *Physical Review B* 70, 054102. URL: <https://link.aps.org/doi/10.1103/PhysRevB.70.054102>, doi:10.1103/PhysRevB.70.054102.
- Simpson, C.J., Aust, K.T., Winegard, W.C., 1971. The four stages of grain growth. *Metallurgical Transactions* 2, 987–991. URL: <https://doi.org/10.1007/BF02664229>, doi:10.1007/BF02664229.
- Srinivasan, S., Cahn, J., 2002. Challenging Some Free-Energy Reduction Criteria for Grain Growth. John Wiley & Sons, Ltd. pp. 1–14. URL: <https://onlinelibrary.wiley.com/doi/abs/10.1002/9781118788103.ch1>, doi:10.1002/9781118788103.ch1, arXiv:<https://onlinelibrary.wiley.com/doi/pdf/10.1002/978>
- Sutton, A., Balluffi, R., 1995. *Interfaces in Crystalline Materials*. Oxford: New York: Clarendon Press. URL: <https://books.google.com.hk/books?id=VLFqAAAACAAJ>.
- Taylor, J.E., Cahn, J., 2007. Shape accommodation of a rotating embedded crystal via a new variational formulation. *Interfaces and Free Boundaries* 9, 493–512. doi:10.4171/IFB/174.
- Thomas, S.L., Chen, K., Han, J., Purohit, P.K., Srolovitz, D.J., 2017. Reconciling grain growth and shear-coupled grain boundary migration. *Nature communications* 8, 1764.

- Thomas, S.L., Wei, C., Han, J., Xiang, Y., Srolovitz, D.J., 2019. Disconnection description of triple-junction motion. *Proceedings of the National Academy of Sciences* 116, 8756–8765. URL: <https://www.pnas.org/content/116/18/8756>, doi:10.1073/pnas.1820789116, arXiv:<https://www.pnas.org/content/116/18/8756.full.pdf>.
- Trautt, Z., Adland, A., Karma, A., Mishin, Y., 2012. Coupled motion of asymmetrical tilt grain boundaries: Molecular dynamics and phase field crystal simulations. *Acta Materialia* 60, 6528 – 6546. URL: <http://www.sciencedirect.com/science/article/pii/S1359645412005472>, doi:<https://doi.org/10.1016/j.actamat.2012.08.018>.
- Upmanyu, M., Hassold, G., Kazaryan, A., Holm, E., Wang, Y., Patton, B., Srolovitz, D., 2002. Boundary mobility and energy anisotropy effects on microstructural evolution during grain growth. *Interface Science* 10, 201–216. URL: <https://doi.org/10.1023/A:1015832431826>, doi:10.1023/A:1015832431826.
- Upmanyu, M., Smith, R., Srolovitz, D., 1998. Atomistic simulation of curvature driven grain boundary migration. *Interface Science* 6, 41–58. URL: <https://doi.org/10.1023/A:1008608418845>, doi:10.1023/A:1008608418845.
- Upmanyu, M., Srolovitz, D., Lobkovsky, A., Warren, J., Carter, W., 2006. Simultaneous grain boundary migration and grain rotation. *Acta Materialia* 54, 1707 – 1719. URL: <http://www.sciencedirect.com/science/article/pii/S135964540500707X>, doi:<https://doi.org/10.1016/j.actamat.2005.11.036>.
- Van Swygenhoven, H., Derlet, P.M., Hasnaoui, A., 2002. Atomic mechanism for dislocation emission from nanosized grain boundaries. *Physical Review B* 66, 024101. URL: <https://link.aps.org/doi/10.1103/PhysRevB.66.024101>, doi:10.1103/PhysRevB.66.024101.
- Von Neumann, J., 1952. *Metal interfaces*. American Society for Metals, Cleveland 108.
- Winning, M., Gottstein, G., Shvindlerman, L., 2001. Stress induced grain boundary motion. *Acta Materialia* 49, 211 – 219. URL:

<http://www.sciencedirect.com/science/article/pii/S1359645400003219>,
doi:[https://doi.org/10.1016/S1359-6454\(00\)00321-9](https://doi.org/10.1016/S1359-6454(00)00321-9).

Winning, M., Gottstein, G., Shvindlerman, L., 2002. On the mechanisms of grain boundary migration. *Acta Materialia* 50, 353 – 363. URL: <http://www.sciencedirect.com/science/article/pii/S1359645401003433>, doi:[https://doi.org/10.1016/S1359-6454\(01\)00343-3](https://doi.org/10.1016/S1359-6454(01)00343-3).

Yang, J.Z., Mao, C., Li, X., Liu, C., 2015. On the cauchyborn approximation at finite temperature. *Computational Materials Science* 99, 21 – 28. URL: <http://www.sciencedirect.com/science/article/pii/S0927025614007988>, doi:<https://doi.org/10.1016/j.commatsci.2014.11.030>.

Zhang, H., Upmanyu, M., Srolovitz, D., 2005. Curvature driven grain boundary migration in aluminum: molecular dynamics simulations. *Acta Materialia* 53, 79 – 86. URL: <http://www.sciencedirect.com/science/article/pii/S1359645404005452>, doi:<https://doi.org/10.1016/j.actamat.2004.09.004>.

Zhang, L., Han, J., Xiang, Y., Srolovitz, D.J., 2017. Equation of motion for a grain boundary. *Physical review letters* 119, 246101.

Zhang, L., Xiang, Y., 2018. Motion of grain boundaries incorporating dislocation structure. *Journal of the Mechanics and Physics of Solids* 117, 157–178.